



OPEN

Detailed three-dimensional fault model of the 2022 M_w 6.6 Luding earthquake reveals seismic hazard potential in the southeastern Tibetan plateau

Fang Xu^{1,2}, Renqi Lu^{1✉}, Jinyu Zhang^{1✉}, Yann Klinger², Yiduo Liu³, Xuhang Yang¹, Guanshen Liu¹, Wei Wang¹ & Zhaowu Guo¹

The detailed 3D fault model and further seismic rupture behavior analysis and fault mechanics simulation based on it are important and meaningful. A strong M_w 6.6 earthquake occurred in Luding, Sichuan, on 5 September 2022, the epicenter was located near the Y-shaped junction of the Xianshuihe Fault Zone (XSHF), the Longmen Shan Fault Zone (LMSF), and the Anninghe Fault Zone (ANHF). To date, a detailed 3D fault model has not been established for this earthquake, preventing a 3D Coulomb stress change (ΔCFS) calculation for further seismic potential analysis. Therefore, first we build a detailed 3D fault model of the earthquake and then we compute ΔCFS in the surrounding areas. Based on 3D modeling technics, we establish a 3D model of the main faults using previously published relocated earthquake catalog and focal mechanism solutions; including the Moxi segment (f_1) of the XSHF, the Daduhe fault (f_2) and two previously unknown faults (f_3 and f_4). The 3D ΔCFS indicates that the strike-slip mainshock of the Luding earthquake significantly triggered two $M > 5$ dip-slip aftershocks. Moreover, it caused a remarkable increase in ΔCFS and hence a notable enhancement in seismic hazard in the northern ANHF.

Keywords Luding M_w 6.6 earthquake, Xianshuihe fault zone, Southeastern Tibetan plateau, 3D fault model, Coulomb stress change, Seismic hazard analysis

The geometry of an active fault controls its seismic potential and segmentation^{1–3} and dictates behaviors such as earthquake nucleation, dynamic rupture, stress triggering, and seismic wave propagation^{4,5}. Therefore, for a nonplanar fault, it is necessary to establish a three-dimensional (3D) fault model to effectively characterize its subsurface complex structures⁶. Accurate geometric shapes of fault systems can better define seismic parameters, such as the fault area and fault length, and have significant impacts on estimating slip rates^{7,8} based on geodetic data and rupture dynamics⁹. The modeling of fault system behavior and dynamic rupture simulations shows that the geometric shape of faults plays a crucial role in fault behavior throughout the entire seismic cycle^{3,10,11}. High-precision data of small earthquakes can intuitively reflect the geometric shapes of active faults through seismic distribution relationships¹².

On 5 September 2022, an M_s 6.8 (M_w 6.6) earthquake occurred in Luding County, Sichuan Province (Fig. 1). It was the strongest earthquake in eastern Tibetan Plateau since the 2017 Jiuzhaigou M 7.0 earthquake. The Luding earthquake occurred at the intersection of the Baryan Har Block, the Sichuan-Yunnan Block, and the South China Block (Fig. 1). It is also near the Y-shaped junction area formed by three large-scale boundary fault zones—the Xianshuihe Fault Zone (XSHF), Longmen Shan Fault Zone (LMSF), and Anninghe Fault Zone (ANHF) (Fig. 1). Surface ruptures from field investigations, surface deformation by InSAR observations, focal mechanism, and relocated aftershocks all show that the seismogenic fault of this earthquake is the Moxi segment of the Xianshuihe Fault Zone, along with the Daduhe fault in the east and some previously unknown faults in the west^{13,14} (Fig. 2).

¹State Key Laboratory of Earthquake Dynamics and Forecasting, Institute of Geology, China Earthquake Administration, Beijing, China. ²Universite Paris Cite, Institut Physique du Globe de Paris, CNRS, Paris, France. ³Key Laboratory of Mountain Hazards and Surface Processes, Institute of Mountain Hazards and Environment, Chinese Academy of Sciences, Chengdu, China. ✉email: lurenqi@163.com; jinyuzhang87@foxmail.com

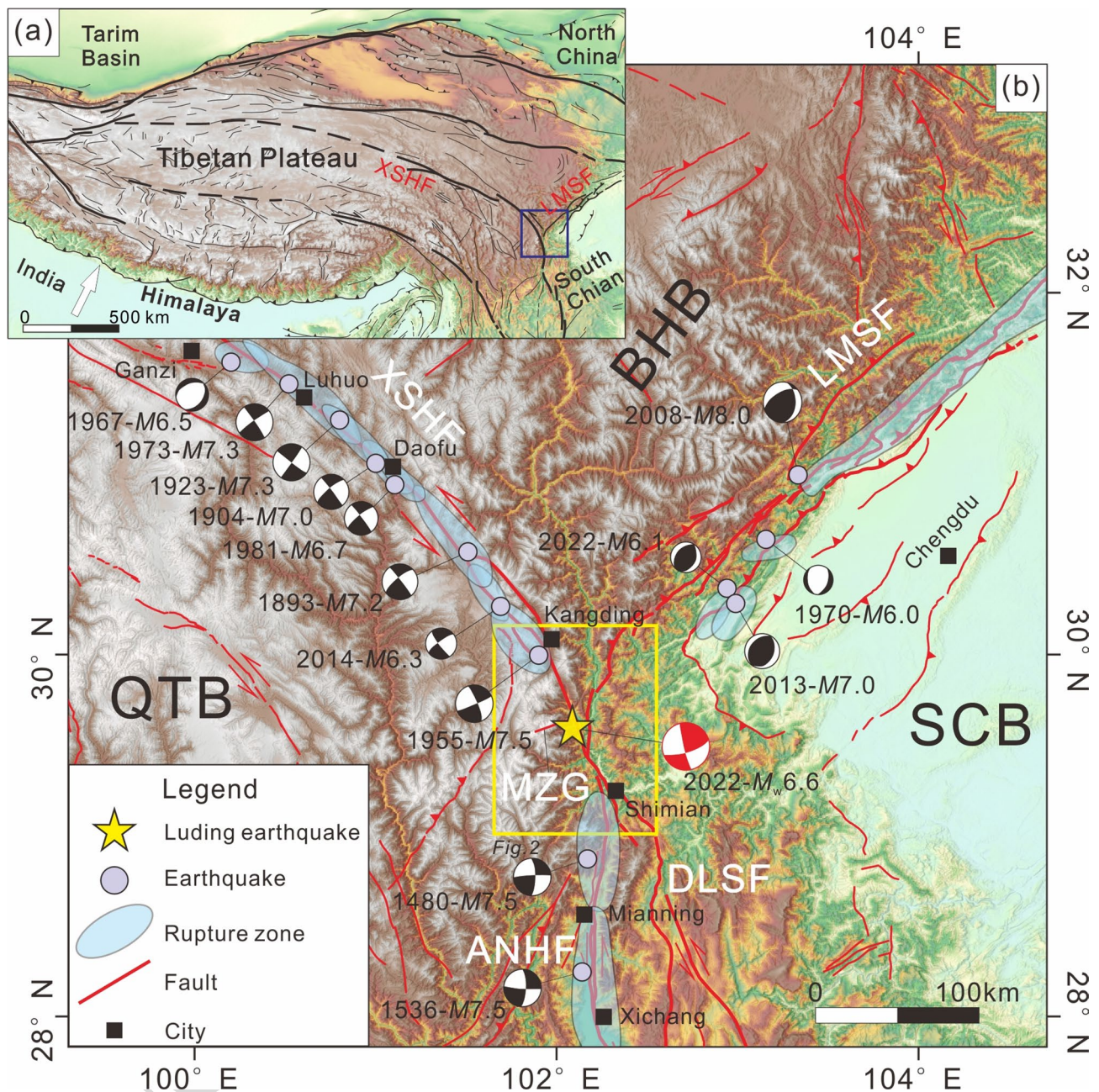


Fig. 1. Topographic and tectonic map of the study area in eastern Tibetan Plateau. (a) Tectonic map of the Tibetan Plateau region. The blue rectangle indicates the study area. (b) Map of main active faults, historical and modern strong earthquakes at the Y-shaped junction area between the Xianshuihe, Longmen Shan, and Anninghe Fault Zones in the Sichuan-Yunnan area. The yellow rectangle indicates the location of Fig. 2. DEM map based on the publicly available Shuttle Radar Topography Mission data with 90 m resolution. Focal mechanism solutions are collected from references^{15–23}. The rupture zone are collected from references²². The focal mechanism solution is the lower hemisphere projection. Abbreviations: ANHF: Anninghe Fault Zone; BHB: Baryan Har Block; DLSF: Daliang Shan Fault Zone; LMSF: Longmen Shan Fault Zone; MZG: Mozigou fault; QTB: Qiangtang Block; SCB: Sichuan Basin; XSHF: Xianshuihe Fault Zone. Figures and maps were generated using QGIS 3.32.1 (<https://download.qgis.org/downloads/>) and CorelDRAW Standard 2024 (<https://www.coreldraw.com/en/product/coreldraw/standard/>).

Due to the lack of data in the early stage after the earthquake, previous studies suggested that the Mozigou fault, which is nearly perpendicular to the Moxi segment, was the seismogenic fault of the aftershocks on the west side of the mainshock^{24,25}. This result however is inconsistent with the focal mechanism solution of the subsequent inversion. After the mainshock of the Luding earthquake, many aftershocks occurred. In particular, two strong aftershocks with a magnitude of Mw 5.1 on 22 October 2022 and Mw 5.4 on 25 January 2023, respectively, occurred on the west side^{14,23}. In contrast to the strike-slip mainshock, both of them were

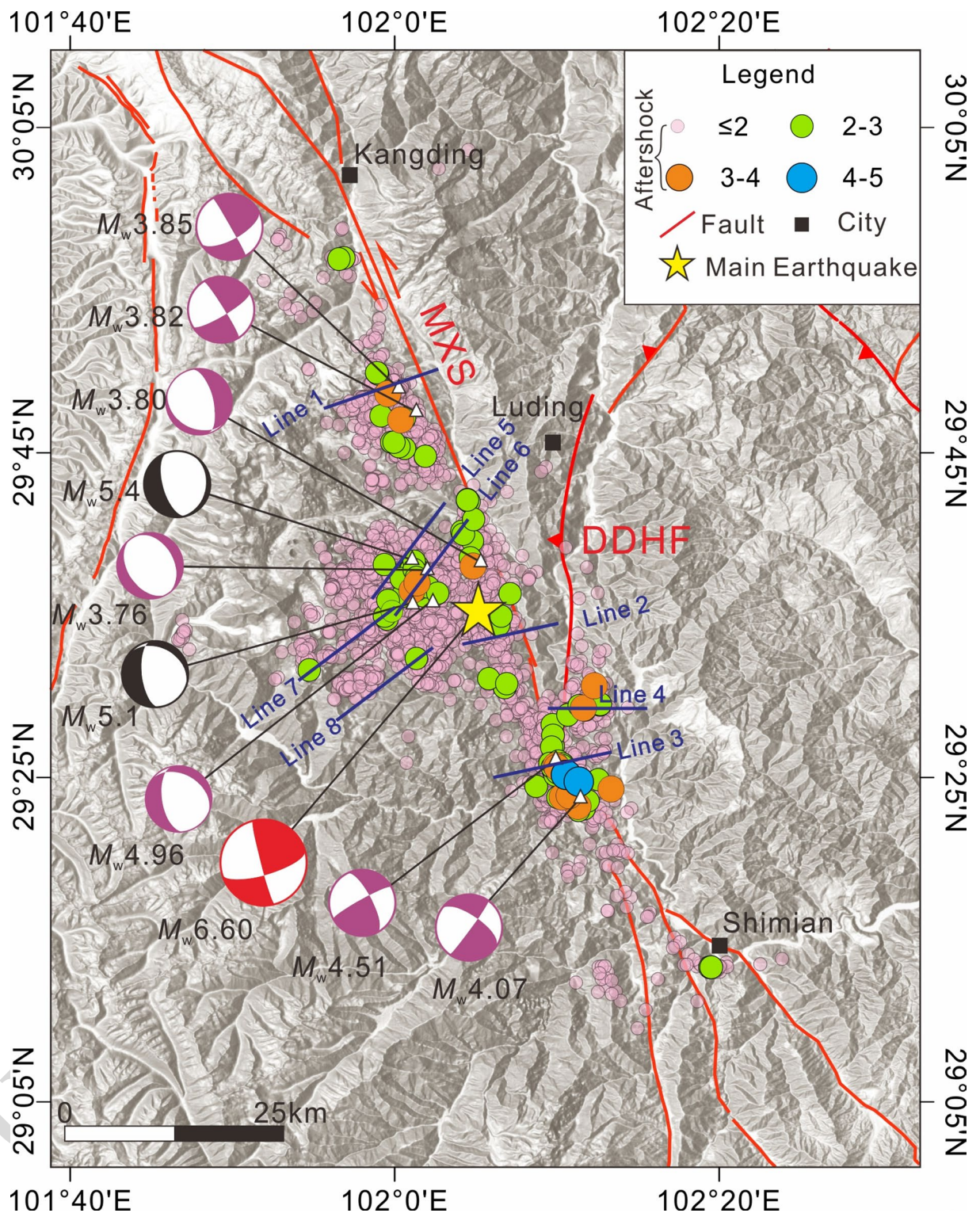


Fig. 2. Distribution of the Luding M_w 6.6 earthquake sequence and focal mechanism solutions. DEM map based on the publicly available Shuttle Radar Topography Mission data with 90 m resolution. The aftershock sequence of the Luding earthquake is from reference²³; focal mechanism solutions in red and black represent the mainshock of the Luding earthquake and the two $M > 5$ aftershocks, respectively²³; the focal mechanism solutions in purple represent seven (7) $M_s \geq 3.0$ aftershocks of the Luding earthquake¹⁴ (same below). The focal mechanism solution is the lower hemisphere projection. The blue line indicates the position of eight representative depth profiles of earthquake clusters in Fig. 4. DDHF: Daduhe fault; MXS: Moxi segment of the Xianshuihe Fault Zone. Figures and maps were generated using QGIS 3.32.1 (<https://download.qgis.org/downloads/>) and CorelDRAW Standard 2024 (<https://www.coreldraw.com/en/product/coreldraw/standard/>).

characterized by normal faulting mechanisms. The relationship between mainshocks and aftershocks with different faulting mechanisms remains unclear. To address this issue, therefore, it is necessary to depict the geometric shape of the seismogenic faults in detail and analyze Coulomb stress change in the Luding earthquake area based on the fine geometric model.

Since 1700, the XSHF has experienced at least sixteen (16) $M \geq 6.5$ earthquakes, including eight $M \geq 7.0$ earthquakes, and coseismic surface ruptures have occurred along almost the entire XSHF (Fig. 1). However, the Moxi segment has not undergone any $M \geq 6.5$ earthquake since the 1786 M 7.3 Kangding earthquake²². The potential seismic hazard after the Luding earthquake on this segment remains unclear. Moreover, there is a seismic gap of 50–60 km long in the southern LMSF between the 2008 Wenchuan M_s 8.0 earthquake and the 2013 Lushan M_s 7.0 earthquake²⁶. The 1st June 2022 Lushan M_s 6.1 earthquake indicates that this seismic gap still has high seismogenic potential¹⁸. Furthermore, the northern ANHF can also be identified as a seismic gap, since it has not experienced an $M \geq 6.5$ earthquake since the 1480 M 7.5 and the 1536 M 7.5 earthquakes. How the occurrence of the 2022 Luding earthquake affects the seismic hazard of the adjacent seismic gaps requires pressingly further research. Based upon two-dimensional fault models, previous researchers computed the Coulomb stress changes caused by this earthquake^{23,24,27}. However, Coulomb stress changes are highly sensitive to geometric variations in faults, and results based on simplified two-dimensional fault models may neglect stress changes at fault bends related to rupture termination or nucleation⁴.

Therefore, this study constructs a detailed, 3D geometric model for the seismogenic fault of the 2022 Luding earthquake by employing 3D modeling techniques on the SKUA-GOCAD software platform and incorporating published results of relocated aftershock catalog and focal mechanism solutions (Fig. 2). We further conduct a 3D Coulomb stress change analysis for the area where the two $M > 5$ aftershocks occurred, as well as the faults in the Y-shaped junction area. Furthermore, in conjunction with long term Coulomb stress and fault coupling characteristics²⁸ this study analyzes the potential seismic hazard in the surrounding two seismic gaps.

Tectonic setting

Since the late Cenozoic, the ongoing convergence between the Indian Plate and the Eurasian Plate has led to extensive extrusion of active blocks in the southeastern Tibetan Plateau²⁹. The Bayan Har Block extrudes eastward but encounters strong resistance from the Yangtze Craton of the South China Block³⁰ leading to the thrust-dominant LMSF³¹ and the Sichuan-Yunnan Block rotates clockwise around the Eastern Himalayan syntaxis³² (Fig. 1a). As a significant boundary fault between these two active blocks, the Xianshuihe-Anninghe-Zemuhe-Xiaojiang Fault Zone exhibits an overall eastward convex arc-shaped structure, coordinating the left-lateral strike-slip motion between the two blocks³³.

The NE-striking LMSF consists of a series of thrust faults and nappe structures (Fig. 1b). Although the overall shortening rate of the LMSF is only approximately 1–2 mm/a^{32,33}, strong earthquakes have occurred frequently in recent decades, including the 2008 Wenchuan M_s 8.0, the 2013 Lushan M_s 7.0 and the 2022 Lushan M_s 6.1 earthquakes.

The NW-striking, 400-km-long XSHF is the boundary fault between the Bayan Har Block and the Sichuan-Yunnan Block in the Tibetan Plateau (Fig. 1b). There is a clockwise deflection of $\sim 10^\circ$ near Kangding. According to the geometry, fault discontinuity, and historical earthquake distribution, the XSHF can be divided into seven segments, including, from NW to SE, the Luhuo, Daofu, Qianning, Yalahe, Salaha, Zheduotang, and Moxi segments. Since the Holocene, the XSHF has been dominated by left-lateral strike-slip with thrust components and is one of the most active tectonic zones on the Chinese continent³⁴. Geodesy shows that the average slip rate of the XSHF has been ~ 9 – 15 mm/a^{32,33}, and geological investigations show that the average slip rate is approximately 10–17 mm/a^{35,36}.

South of the XSHF, the ANHF exhibits an almost N-S trend³⁷ (Fig. 1b). Geodesy shows a slip rate of ~ 5 – 7 mm/a³⁸. No strong earthquake has been recorded in the fault zone since the 1480 M 7.5 earthquake and the 1536 M 7.5 earthquake, showing an obvious “seismic gap”.

Data and method

An accurately relocated aftershock catalog can be used to constrain the geometry of the fault plane and is the first and foremost data source for establishing a 3D model of a seismogenic fault³⁹. This study collects 5269 aftershocks that occurred within 34 days after the mainshock of the Luding earthquake, as well as the focal mechanism solutions of the two $M > 5$ aftershocks relocated by Zhang et al. (2023) (Figs. 2 and 3; Table 1). This aftershock catalog, as well as the focal mechanism solutions, obtained by relocation using the HypoDD method⁴⁰ is based on the complete waveforms of 34 stations within 120 km of the epicenter, 13 of which are located within 50 km of the epicenter. It has lateral and vertical uncertainties of 190 m and 300 m respectively, with an average root mean square (RMS) residual of 22 ms. This study analyzes the cluster characteristics of the aftershock catalog in 3D space using the SKUA-GOCAD platform. We build a series of vertical profiles perpendicular to the strike of the aftershock cluster (Fig. 2) and map the fault traces on each profile based on the linear distribution characteristics of the aftershock cluster⁴¹. We then construct a 3D fault plane of the Luding earthquake. The focal mechanism solutions of seven $M_s > 3$ earthquakes calculated by Yi et al. (2023), using fixed station waveform data within 350 km of the epicenter and the Cut and Paste (CAP) waveform inversion, are also collected to constrain the fault plane occurrence (Figs. 2 and 3; Table 1).

The summation of the shear and normal stress changes provides the Coulomb stress change (ΔCFS)⁴³ failure is encouraged if ΔCFS is positive and discouraged if negative⁴⁴. We conducted our study using the expression.

where τ is the shear stress, σ_N is the normal stress and μ' is the apparent coefficient of friction⁴⁵.

To further quantitatively understand the seismogenic environment and seismic hazard in the area adjacent to the Luding earthquake, we calculate the ΔCFS on nearby faults induced by the Luding mainshock. We also incorporate the coupling data of the Y-shaped junction fault inverted by Li et al. (2023) using geodetic data,

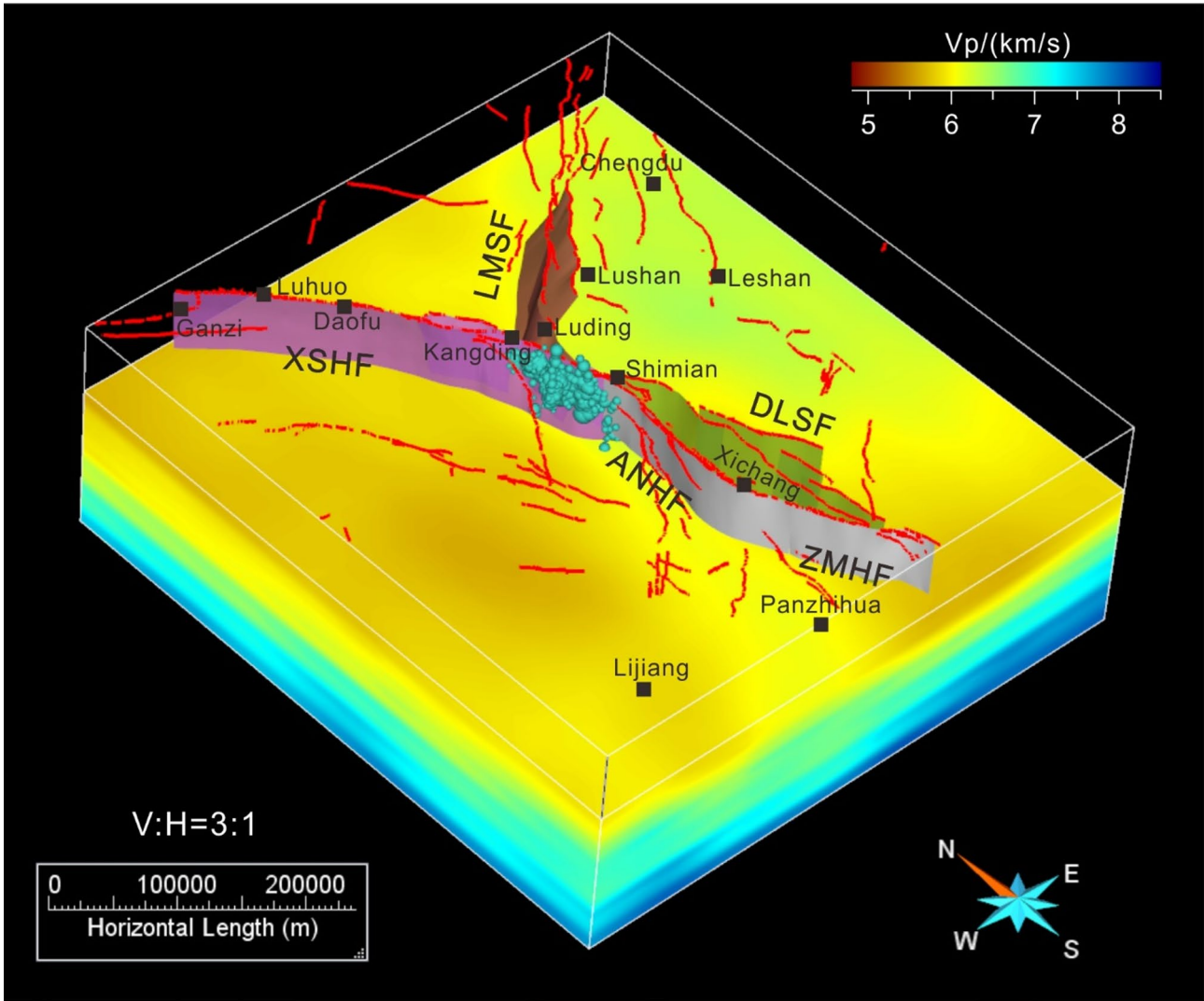


Fig. 3. Three-dimensional fault model, velocity model, and distribution of earthquakes in the Luding earthquake catalog in the Y-shaped junction area. The P-wave velocity model is from reference⁴² and the Y-shaped junction fault model is from the China Seismic Experimental Site. For visualization purposes, the vertical exaggeration is 3x. Figure were generated using SKUA-GOCAD 2017 (<https://www.aspentech.com/en/products/sse/aspen-skua>) and CorelDRAW Standard 2024 (<https://www.coreldraw.com/en/product/coreldraw/standard/>).

Time(yyyy/mm/dd)	Location		Depth (km)	M_w	Nodal Plane I			Nodal Plane II			Sources
	X (°)	Y (°)			Strike (°)	Dip (°)	Rake (°)	Strike (°)	Dip (°)	Rake (°)	
2022/9/5	102.086	29.589	6.5	6.60	74	73	176	166	86	17	[23]
2023/1/25	102.017	29.641	6.0	5.40	164	64	-103	11	29	-66	
2022/10/22	102.018	29.597	5.0	5.10	173	66	-62	300	36	-136	
2022/9/5	102.191	29.397	4.0	4.07	36	86	-158	304	68	-4	[14]
2022/9/6	102.088	29.638	3.5	3.80	120	35	-130	345	64	-66	
2022/9/6	102.033	29.629	2.5	3.76	146	47	-93	330	43	-87	
2022/9/7	102.165	29.436	7.5	4.51	241	84	163	333	73	6	
2022/9/7	102.005	29.815	5.0	3.85	61	67	-178	330	88	-23	
2022/9/8	102.022	29.792	5.5	3.82	59	79	-175	328	85	-11	
2022/10/22	102.04	29.599	5.0	4.96	302	41	-130	170	60	-61	

Table 1. Focal mechanism solutions of the Luding earthquake sequence obtained from different sources.

to investigate (1) why the strike-slip mainshock has dip-slip aftershocks and (2) the influence of the Luding earthquake on the seismogenic potential of the two seismic gaps in the southern LMSF and the northern ANHF. Numerous coseismic slip models have been developed for the Luding earthquake^{24,47}. We adopt the model proposed by Li et al. (2022), as it is derived from a joint inversion of multiple geophysical datasets—including GPS measurements, seismic station records, and InSAR-derived static displacements—and incorporates complex fault system. We project it onto the 3D fault model of Moxi fault established in this study, which is interpreted as the seismogenic fault. And then, on the Relax platform⁴⁸ we use the fault models of the southern LMSF, ANHF, and Daliang Shan Fault Zone published by the China Seismic Experimental Site (Fig. 3) as the receiver faults to obtain the Δ CFS result. The Poisson's ratio, friction coefficient, and Young's modulus are set to 0.25, 0.4, and 80 GPa respectively.

Results and discussion

The 3D model of the seismogenic fault

Fault trace mapping

The aftershock sequence of the Luding earthquake can be divided into four distinct clusters in 3D space: (1) a cluster distributed along the mainshock seismogenic fault, i.e. the Moxi segment of the XSHF; (2) a cluster along the Daduhe fault; and (3) two sub-parallel aftershock clusters to the west of the mainshock (Fig. 2, Supplementary Movie S1). To characterize the 3D geometry of the fault planes associated with each aftershock cluster, we construct a series of vertical depth profiles perpendicular to the trend of these clusters, and the aftershocks are projected onto the profiles based on their distribution density within a given range: 2 km for the first two clusters and 1.5 km for the latter two clusters. In total, we establish 56 profiles, of which 8 representative profiles are presented here to illustrate the characteristics of the aftershock clusters on different seismogenic fault segments of the Luding earthquake (Figs. 2 and 4).

Lines 1–3 are located in the northern, central, and southern parts of the Moxi segment (f_1) (Figs. 4a–c). The linear relationship in Line 3 is notably better than those in Line 1 and Line 2. It is evident that the fault dips to the northeast, consistent with the nodal plane of the focal mechanism. The aftershock distribution along Line 2 appears relatively scattered, and we interpret the fault plane as southwest-dipping when considering the focal mechanism solution of the mainshock and the distribution of aftershocks to the north and south of Line 2. Similarly, the northern fault plane is found to be northeast-dipping.

On the eastern side of the mainshock, the aftershock cluster generated by the Daduhe fault (f_2) exhibits a lower number of aftershocks, and this region lacks constraints from focal mechanism solutions (Fig. 4d). Combining previous geological surface investigations on this fault, we determine that the fault dips to west-southwest⁴⁹.

The aftershocks on the western side of the Moxi segment can be divided into two sub-parallel clusters and are interpreted as faults f_3 and f_4 . Focal mechanism solutions show that these faults are normal faults, with little strike-slip components. Considering the consistency of the focal mechanism solutions within the clusters, we interpret both fault planes as northwest-striking, southwest-dipping, with top-down-to-the-southwest sense of motion (Figs. 4e–h). This interpretation also aligns with the northwest-trending valleys within the Gongga Mountains in this region.

3D fault model

We build the 3D model for the four seismogenic faults based on the interpretation of 56 profiles (Fig. 5a, Supplementary Movie S2). The fault models (Figs. 5b–e) reveal that the depth constrained by the seismic clusters is up to approximately 15 km for the Moxi segment of the XSHF and the Daduhe fault. For the secondary faults f_3 and f_4 , the aftershocks are distributed at shallower depths, so the deepest depth constraint for these faults is approximately 12 km.

The Moxi segment (f_1) (Figs. 5a, b) has an approximate length of 55 km and an area of approximately 860 km². It exhibits an overall NNW-striking, sub-vertical (77°–89°) attitude. Along the strike of the fault plane, the dip direction changes from NE in the north to SW in the central, and then back to NE in the south. The aftershocks in the northern and central parts of the fault are mainly concentrated within a depth range of 2–7 km, with a higher number of shallow aftershocks. In the southern region, aftershocks are primarily distributed at depths of 3–15 km, and the distribution is relatively uniform.

The Daduhe fault (f_2) (Figs. 5a, c) is approximately 14 km long, and the fault plane has an area of approximately 213 km². It strikes nearly due N and dips to the SWW overall, with a steep average dip angle of 88°. However, it is crucial to exercise caution when using the dip angle range and variations in the 3D model of this fault due to its relatively weak activity during the Luding earthquake and the limited number of associated aftershocks.

The aftershock clusters on the western side of the Moxi segment have provided a more substantial number of aftershocks and have effectively constrained the geometry of f_3 and f_4 (Figs. 5a, d, e). The 3D model indicates that these two fault segments are approximately 10 km and 8 km long, respectively, with an area of approximately 137 km² and 119 km² respectively. Both f_3 and f_4 exhibit sub-parallel, NW-strike and dip to the SW, with dip angles of 55°–64° for f_3 and 52°–66° for f_4 . The geometric characteristics of these two fault segments are highly similar. However, given that faults f_3 and f_4 were not identified in previous field investigations, their near-surface geometries should be treated with caution.

In the regions where the aftershocks are sparse, the exact intersections or connections among the four faults are not entirely clear. Additionally, because the aftershock catalog provides relative positions, the fault models of the Luding earthquake may deviate from the surface fault traces determined through active fault detection. However, this deviation does not hinder the characterization of the fault geometry.

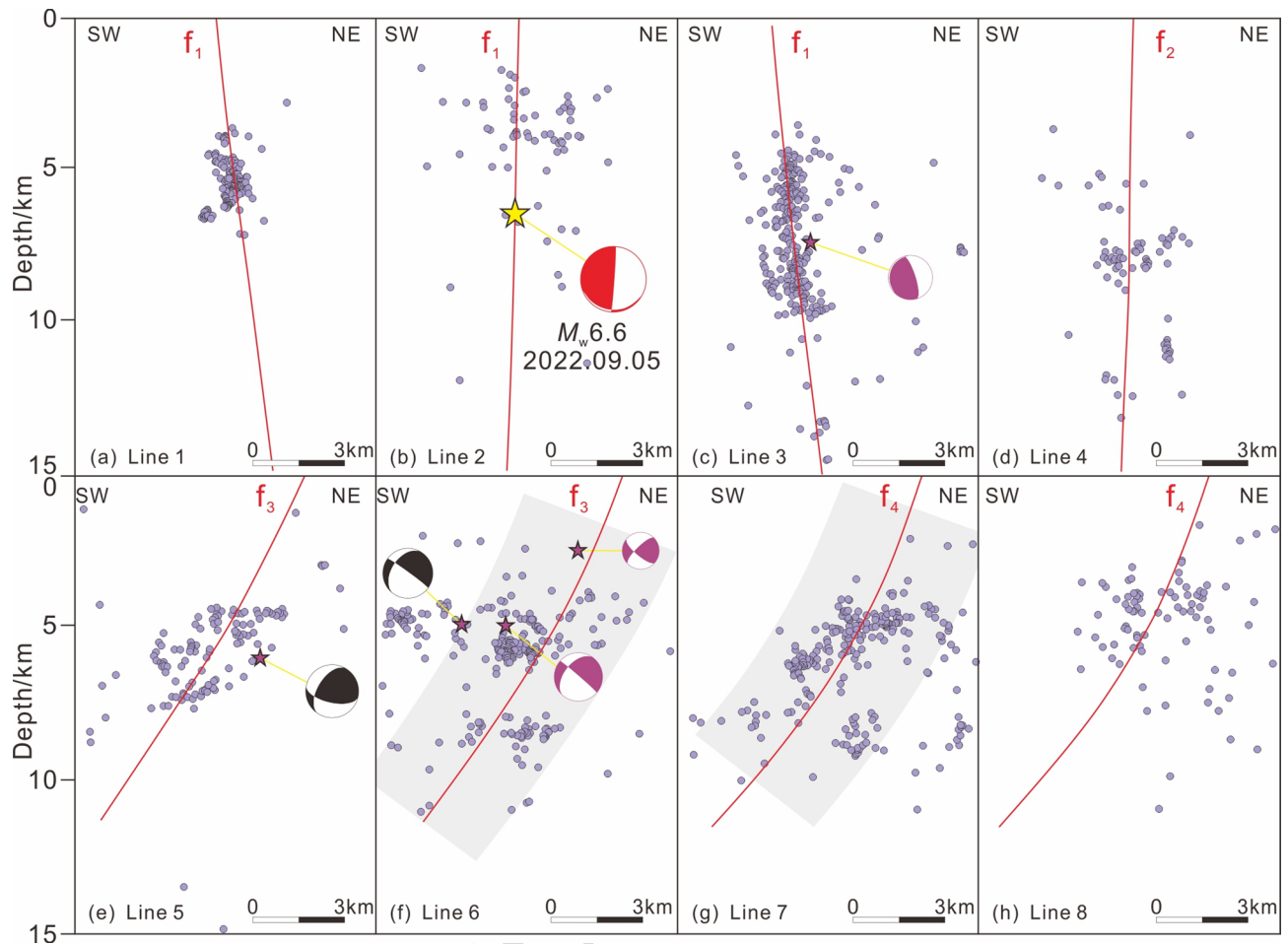


Fig. 4. Eight representative depth profiles of vertically-oriented earthquake clusters, lateral aftershock projection, and interpreted fault traces. (a–c) Lines 1–3 are perpendicular to the Moxi segment of the XSHF (f_1), and (d) Line 4 is perpendicular to the Daduhe fault (f_2). Aftershocks within a 2 km range on both sides of the profiles are projected on the diagrams. (e–h) Lines 5–6 and 7–8 are perpendicular to two newly identified faults, f_3 and f_4 , to the west of the mainshock. Aftershocks within a 1.5 km range on both sides of the profiles are projected on the diagrams. The gray areas represent the data range, and the red lines represent the fault traces on the profiles. Figure were generated using SKUA-GOCAD 2017 (<https://www.aspentech.com/en/products/sse/aspens-sku>) and CorelDRAW Standard 2024 (<https://www.coreldraw.com/en/product/coreldraw/standard/>).

The triggering effect of the luding earthquake on aftershocks

Seismic triggering refers to the process in which the stress changes associated with an earthquake can accelerate or delay seismic activity in surrounding areas or trigger other earthquakes at greater distances⁴³. Coulomb stress loading on the surrounding faults caused by a strong earthquake event is one of the important factors triggering an aftershock⁵⁰. For example, the regional stress changes caused by the 1992 Landers M_w 7.3 earthquake in the United States triggered the 1992 Big Bear M_w 6.3 earthquake only 3.5 h afterward⁵¹ and also the 1999 Hector Mine M_w 7.1 earthquake⁵². The 2008 Wenchuan M_s 8.0 earthquake had an obvious triggering effect on most of its strong aftershocks, and may trigger the 2013 Lushan M_s 7.0 earthquake^{53,54}.

After the mainshock of the Luding earthquake, two $M > 5$ aftershocks occurred in the seismic area, namely, the M_w 5.1 aftershock on 22 October 2022 and the M_w 5.4 aftershock on 25 January 2023²³. Their seismogenic faults are the branch faults f_3 and f_4 west of the Moxi segment. In contrast to the strike-slip mechanism of the mainshock, these two aftershocks exhibited normal faulting characteristics. Before the Luding earthquake, the 7-year earthquake catalog shows these two branch faults had obvious microseismic activities⁵⁵ but none of the earthquakes were greater than M 5. Hence, this section aims to explore whether there is a stress-triggering effect between the Luding earthquake and its strong aftershocks with different rupture mechanisms.

We use f_1 as the seismogenic fault and f_2 – f_4 as the receiver faults to calculate the Coulomb stress changes (ΔCFS). The result (Fig. 6) shows that the ΔCFS on f_3 and f_4 is generally positive. The range of the ΔCFS on f_1 is 0.27–1.59 MPa, and for f_3 , the range is –0.07–1.37 MPa. The ΔCFS on ~90% of the fault surface is ≥ 0.01 MPa. Therefore, for f_3 and f_4 , the ΔCFS on most fault planes far exceeds the threshold (0.01 MPa) of triggering effects^{56,57}. Meanwhile, the epicenters of the two strong aftershocks coincide with regions of high positive ΔCFS .

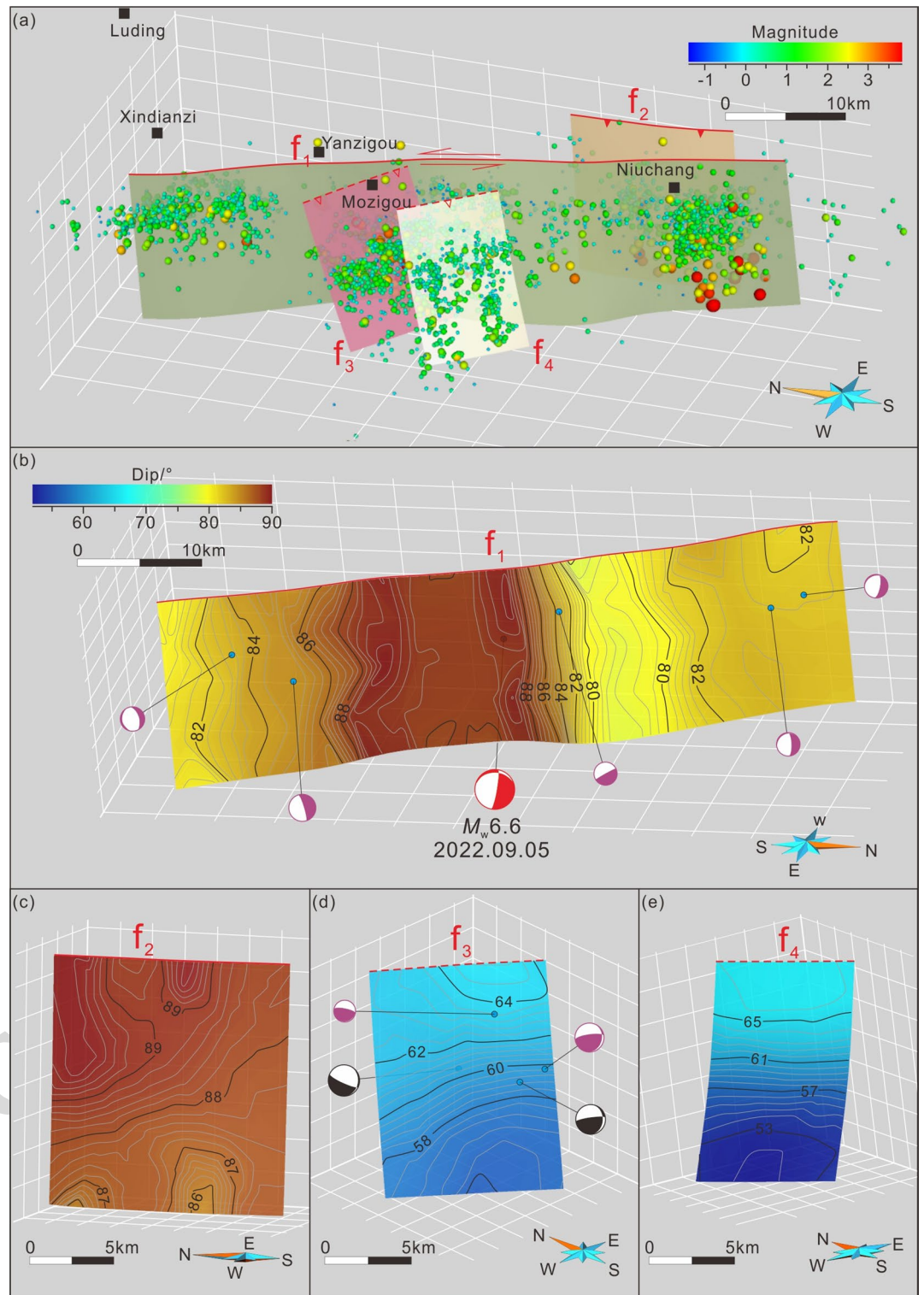


Fig. 5. Geometric representations of the 3D fault model of the 2022 Luding M_w 6.6 Earthquake based on the aftershock catalog. (a) Overall 3D fault model. Solid triangles represent thrust faults, and hollow triangles represent normal faults. (b–e) Detailed representation of the four seismogenic faults, on which the contours represent the dips. The color bar for the dip angles of all four figures is shown in the upper left corner of (b). Figure was generated using SKUA-GOCAD 2017 (<https://www.aspentech.com/en/products/sse/aspken-skua>) and CorelDRAW Standard 2024 (<https://www.coreldraw.com/en/product/coreldraw/standard/>).

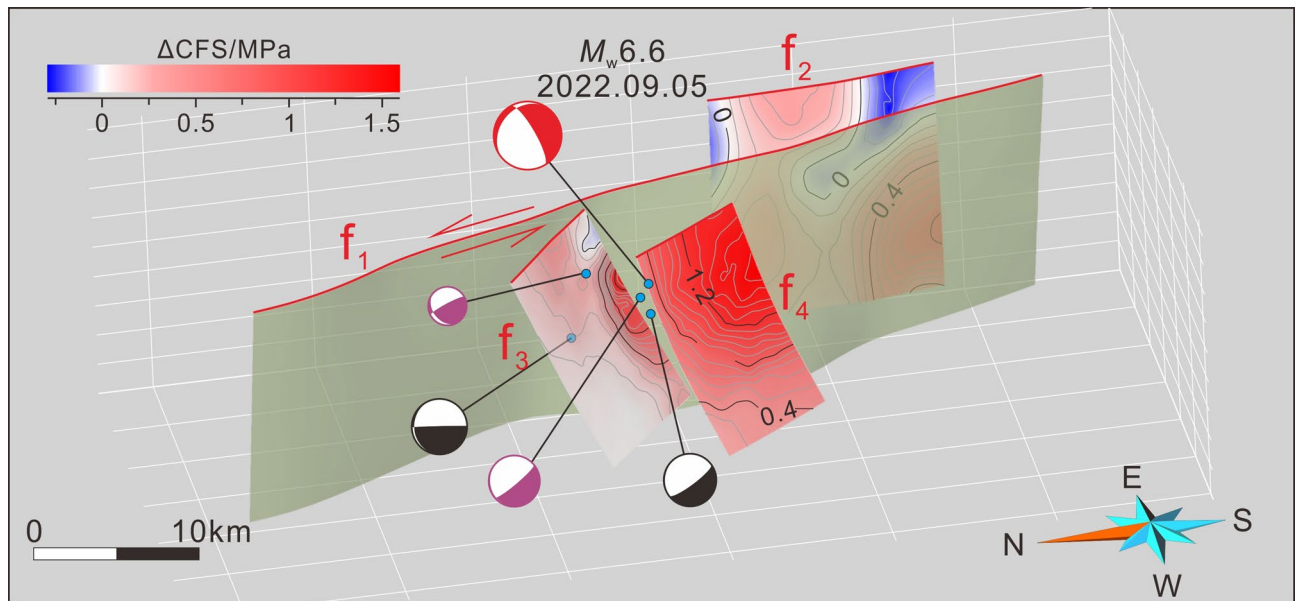


Fig. 6. The Coulomb stress change (ΔCFS) on the branch faults f_2 , f_3 , and f_4 caused by the mainshock of the 2022 Luding earthquake. The black and gray lines on the fault surfaces represent contours of Coulomb stress changes. The red and black focal mechanism solutions denote the mainshock of the Luding earthquake and the two $M > 5.0$ aftershocks, respectively²³; the purple ones represent $M_s \geq 3.0$ aftershocks in the Luding earthquake¹⁴. Figure were generated using SKUA-GOCAD 2017 (<https://www.aspentech.com/products/engineering/skua-gocad>), Relax 1.0.7 (<https://github.com/geodynamics/relax/releases/tag/1.0.7>) and CorelDRAW Standard 2024 (<https://www.coreldraw.com/en/product/coreldraw/standard/>).

on faults f_3 and f_4 (Fig. 6). Although the Coulomb stress distribution patterns are generally similar if we set the two branch faults (f_3 and f_4) as normal faults and strike-slip faults (with rake angles of -90° and 0° , respectively, and consistent 3D fault geometries), respectively, the normal fault exhibits slightly higher positive Coulomb stress values than the strike-slip fault. We infer that this is one of the main reason why the Luding strike-slip earthquake can trigger dip-slip aftershocks. And the higher ΔCFS on these two fault planes is consistent with the larger number of aftershocks in this area (Fig. 2).

Unlike f_3 and f_4 , positive and negative values of ΔCFS appear alternately on the Daduhe fault (f_2), ranging from -0.29 to 0.85 MPa (Fig. 6). The ΔCFS values are generally lower than those on the two branch faults, which is also consistent with the fact that there are fewer aftershocks around this fault (Fig. 2). The consistency of the distribution of ΔCFS values on the fault plane and the number of aftershocks suggests that our calculated results are relatively reliable.

Seismic hazard analysis in surrounding fault zones

The seismic gap in the southern LMSF exhibits the features of low b-values and relatively high seismic apparent stress and has the stress conditions to trigger a moderate-strong earthquake⁵⁸ which is proven by the occurrence of the M_s 6.1 Lushan earthquake in 2022. From the perspective of the seismic moment deficit, a previous study states that this area has the seismic potential to generate a M_w 7.2–7.3 earthquake²⁶ and the seismic moment released by the 2022 M_s 6.1 Lushan earthquake is not enough to fill the above deficit (Fig. 1b). The northern ANHF is a “seismic gap” area²² (Fig. 1b), and the elapsed times of the latest strong earthquakes, the 1480 M 7.5 earthquake and the 1536 M 7.5 earthquake, have reached 543 a and 460 a, respectively. Paleoseismic research shows that the recurrence interval of strong earthquakes in the northern ANHF is 520–660 a³⁷. Hence, this seismic gap is very close to or has entered the recurrence stage. This area has the potential for a M_w 7.2 earthquake⁵⁹. These two fault zones have a high degree of coupling²⁸ (Fig. 7), so the strains received by the faults within a depth of approximately 10 km in the southern LMSF and a depth of approximately 20 km in the ANHF have all accumulated and are basically not released through creep^{28,60}. We envision that the energy accumulated in this area have not been released because this area lacks strong earthquakes.

Therefore, the southern LMSF and the northern ANHF have high seismogenic potential. What impact did the Luding M_w 6.6 earthquake have on these two fault zones? Coulomb stress changes along the North Anatolian Fault Zone in Türkiye indicate that the İzmit region was located in a positive ΔCFS area with elevated seismic hazard, where the 1999 İzmit M_w 7.4 earthquake subsequently occurred⁶¹. Hence, calculating the ΔCFS induced by strong seismic events in the surrounding fault zones can aid in a more precise evaluation of seismic hazard^{49,62,63}. We use the Moxi segment of the XSHF as the seismogenic faults and the southern LMSF, the ANHF, and the Daliang Shan Fault Zone as the receiver faults to calculate the ΔCFS (Fig. 8).

The results (Fig. 8) indicate that most faults are primarily within the positive ΔCFS region, except for a small area in the northern ANHF, which exhibits a noticeable negative ΔCFS , corresponding to the fault rupture

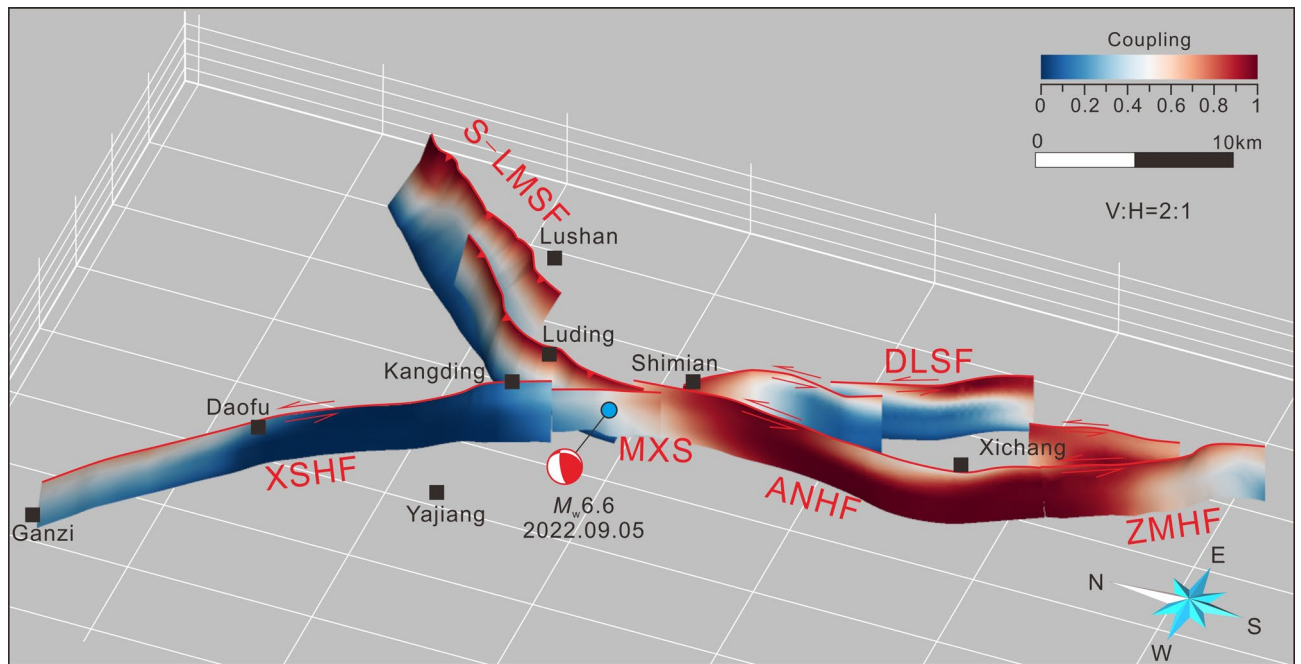


Fig. 7. Interseismic coupling distribution of the main fault zone in the Y-shaped junction area of the three main fault zones. The coupling data are from reference²⁸. ANHF: Anninghe Fault zone; DLSF: Daliang Shan Fault Zone; S-LMSF: southern Longmen Shan Fault Zone; XSHF: Xianshuihe Fault Zone; ZMHF: Zemuhe Fault Zone. Figure were generated using SKUA-GOCAD 2017 (<https://www.aspentech.com/en/products/sse/aspen-skua>) and CorelDRAW Standard 2024 (<https://www.coreldraw.com/en/product/coreldraw/standard/>).

unfavorable zone. However, only the southernmost LMSF and the northernmost ANHF surpass the ΔCFS threshold for triggering an earthquake (0.01 MPa). In comparison to another area, the northern terminus of the ANHF has a significantly higher ΔCFS value, reaching 0.43 MPa. The long-term accumulation ΔCFS along the Anninghe fault zone — incorporating co-seismic, post-seismic, and interseismic tectonic loading — indicates that the northern segment has accumulated over 1 MPa of positive ΔCFS over the past centuries^{17,64}. Based on our calculations, even in the co-seismic stress-shadow (negative ΔCFS) area following the Luding earthquake, the accumulated ΔCFS remains above 0.8 MPa, while in regions with co-seismic positive ΔCFS , the accumulated ΔCFS reaches nearly 1.5 MPa. Given the high level of coupling and its proximity to the recurrence interval of strong earthquakes, we suggest that the ΔCFS induced by the Luding earthquake has significantly elevated the seismic hazard of the northern ANHF.

Conclusion

We have established a three-dimensional model of the seismogenic fault associated with the 2022 Luding M_w 6.6 earthquake using the aftershock catalog. The three-dimensional fault model contains the Moxi segment of the Xianshuihe Fault (f_1), the Daduhe Fault Zone (f_2), and two previously unknown faults, named f_3 and f_4 in this article.

Based on the new 3D fault model, we have calculated the three-dimensional Coulomb stress changes (ΔCFS) in this region. Our results suggest that the ΔCFS on f_3 and f_4 can reach a maximum of 1.59 MPa, evidently triggering the two strong $M > 5$ aftershocks nearby. It also shows that only the northern Anninghe Fault Zone has reached the earthquake-triggering threshold (0.01 MPa), with the maximum value reaching 0.43 MPa, resulting in a significant increase in seismic hazard. Our study demonstrates that incorporating a three-dimensional model in the calculation of Coulomb stress changes leads to notably improved accuracy in assessing the seismic triggering effects following great earthquakes, as well as their influence on seismic gaps.

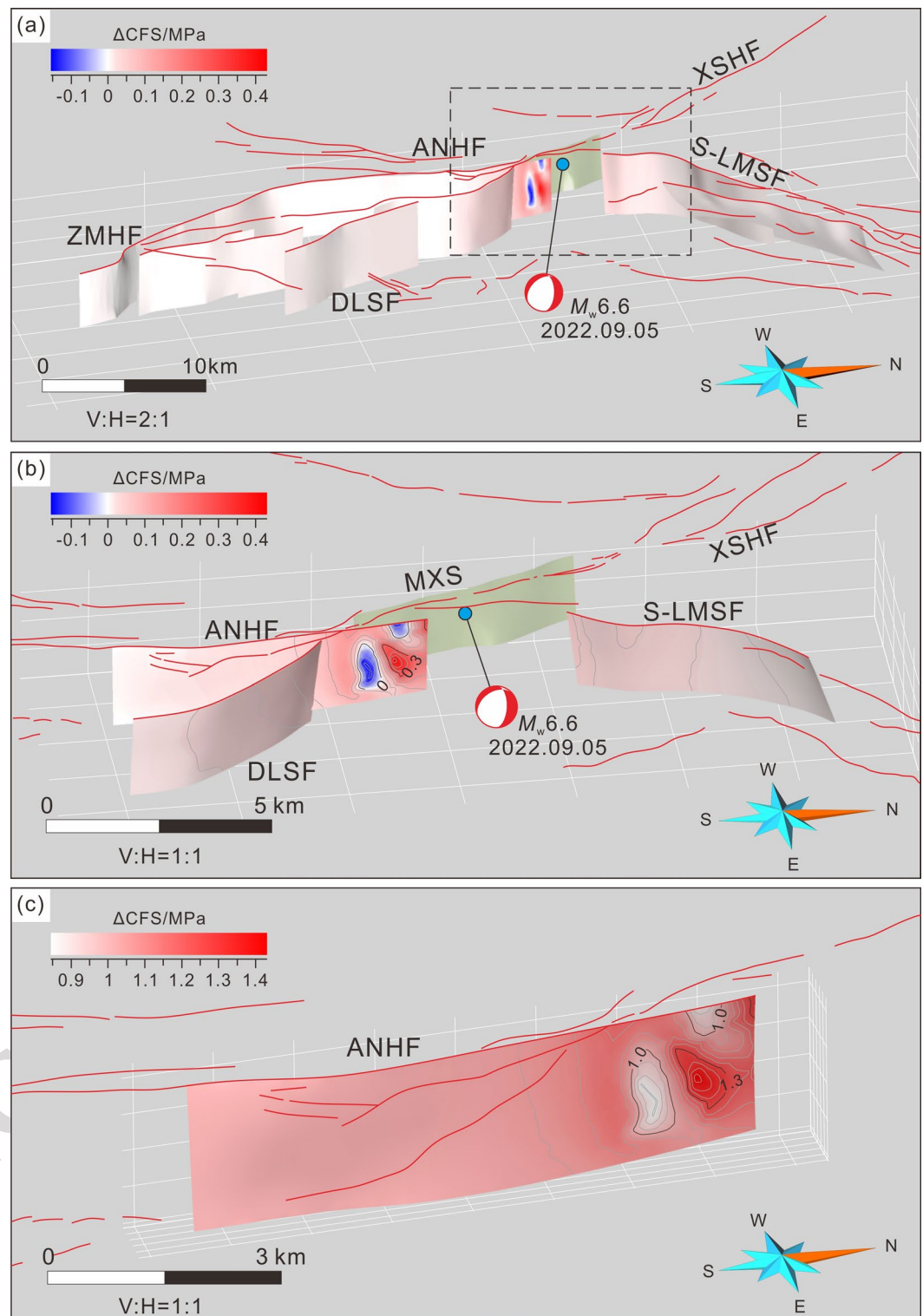


Fig. 8. Coulomb stress change (ΔCFS) on faults in the Y-shaped junction area of the main fault zones induced by the mainshock of the 2022 Luding earthquake. **(b)** Enlarged view of the dashed box in **(a)**. **(c)** Cumulative Coulomb stress in the northern ANHF, incorporating results from reference^{17,64}. The black and gray lines on fault surfaces represent contours of Coulomb stress changes. Figure were generated using SKUA-GOCAD 2017 (<https://www.aspentech.com/products/engineering/skua-gocad>), Relax 1.0.7 (<https://github.com/geodynamics/relax/releases/tag/1.0.7>) and CorelDRAW Standard 2024 (<https://www.coreldraw.com/en/product/coreldraw/standard/>).

Data availability

The aftershock relocation catalog, P-wave velocity data and the three-dimensional fault model used in this study are publicly accessible from the following repositories: (1) Aftershock relocation catalog: https://github.com/YijianZhou/Seismic-Catalog/blob/main/Zhang_SRL-2023_Luding_CENC-ct-cc.ctlg. (2) P-wave velocity data: <https://github.com/liuyingustc/SWChinaCVM-V2.0>. (3) Three-dimensional fault model except f1-f4: <http://www.cses.ac.cn/sjcp/ggmx/2024/609.shtml>. The focal mechanism solutions data are included in the main text of Zhang et al. (2023a), and Yi et al. (2023). The interseismic coupling data that support the findings of this study are available from Li et al. (2023) but restrictions apply to the availability of these data, which were used under license for the current study, and so are not publicly available. Data are however available from the corresponding author upon reasonable request and with permission of Li et al. (2023).

Received: 16 May 2025; Accepted: 10 July 2025

References

- Deng, Q. D. & Wen, X. Z. A review on the research of active tectonics—History, progress, and suggestions (in Chinese). *Seismology Geol.* **30**, 1–30 (2008).
- Guyonnet-Benaize, C. et al. Three-dimensional structural modeling of an active fault zone based on complex outcrop and subsurface data: the middle Durance fault zone inherited from polyphase Meso-Cenozoic tectonics (southeastern France). *Tectonics* **34**, 265–289 (2015).
- Klinger, Y. Relation between continental strike-slip earthquake segmentation and thickness of the crust. *Journal Geophys. Research: Solid Earth*, **115**, (2010).
- Mildon, Z. K., Roberts, G. P., Walker, F., Toda, S. & J. P., & Coulomb pre-stress and fault bends are ignored yet vital factors for earthquake triggering and hazard. *Nat. Commun.* **10**, 2744 (2019).
- Ross, Z. E., Cochran, E. S., Trugman, D. T. & Smith, J. D. 3D fault architecture controls the dynamism of earthquake swarms. *Science* **368**, 1357–1361 (2020).
- Plesch, A. et al. Community fault model (CFM) for Southern California. *Bull. Seismol. Soc. Am.* **97**, 1793–1802 (2007).
- Griffith, W. A. & Cooke, M. L. How sensitive are Fault-Slip rates in the Los Angeles basin to tectonic boundary conditions?? *Bull. Seismol. Soc. Am.* **95**, 1263–1275 (2005).
- Meade, B. J. & Hager, B. H. Spatial localization of moment deficits in Southern California. *Journal Geophys. Research: Solid Earth*, **110** (2005).
- Oglesby, D. D. The dynamics of Strike-Slip Step-Overs with linking Dip-Slip faults. *Bull. Seismol. Soc. Am.* **95**, 1604–1622 (2005).
- Marshall, S. T., Cooke, M. L. & Owen, S. E. Interseismic deformation associated with three-dimensional faults in the greater Los Angeles region, California. *Journal Geophys. Research*, **114** (2009).
- Duru, K. & Dunham, E. M. Dynamic earthquake rupture simulations on nonplanar faults embedded in 3D geometrically complex, heterogeneous elastic solids. *J. Comput. Phys.* **305**, 185–207 (2016).
- Li, L. G. et al. Three-Dimensional fault model and activity in the Arc-Shaped tectonic belt in the Northeastern margin of the Tibetan plateau. *Front. Earth Sci.* **10**, 893558 (2022).
- Liu, Z. M. et al. Auto-building of aftershock sequence and seismicity analysis for the 2022 luding, sichuan, Ms6.8 earthquake (in Chinese). *Chin. J. Geophys.* **66**, 1976–1990 (2023).
- Yi, G. X. et al. Seismogenic structure of the 5 September 2022 Sichuan Luding Ms6.8 earthquake sequence (in Chinese). *Chin. J. Geophys.* **66**, 1363–1384 (2023).
- China Earthquake Disaster Prevention Center. *Catalog of Modern Earthquakes in China from 1912 To 1990 AD, Ms ≥ 4.7* (Science and technology of China, 1999).
- Yi, G. X. et al. Focal mechanism and tectonic deformation in the seismogenic area of the 2013 Lushan earthquake sequence, Southwestern China (in Chinese). *Chin. J. Geophys.* **59**, 3711–3731 (2016).
- Xu, J., Shao, Z. G., Liu, J. & Ji, L. Y. Coulomb stress evolution and future earthquake probability along the Eastern boundary of the Sichuan-Yunnan block (in Chinese). *Chin. J. Geophys.* **62**, 4189–4213 (2019).
- Lu, R. Q. et al. Detailed structural characteristics of the 1 June 2022 Ms 6.1 Sichuan Lushan strong earthquake (in Chinese). *Chin. J. Geophys.* **65**, 4299–4310 (2022).
- Li, Z. G. et al. Re-evaluating seismic hazard along the Southern longmen shan, china: insights from the 1970 Dayi and 2013 Lushan earthquakes. *Tectonophysics* **717**, 519–530 (2017).
- Papadimitriou, E., Wen, X. Z., Karakostas, V. & Jin, X. S. Earthquake triggering along the Xianshuihe fault zone of Western sichuan, China. *Pure. Appl. Geophys.* **161**, 1683–1707 (2004).
- USGS. https://earthquake.usgs.gov/earthquakes/eventpage/usp000g650/moment-tensor?source=us&code=pde20080512062801570_19_C_UCMTtr (accessed 14 July 2023)
- Wen, X. Z., Ma, S. L., Xu, X. W. & He, Y. N. Historical pattern and behavior of earthquake ruptures along the Eastern boundary of the Sichuan-Yunnan faulted-block, Southwestern China. *Phys. Earth Planet. Inter.* **168**, 16–36 (2008).
- Zhang, L. et al. Mw 6.6 Luding, China, Earthquake: A Strong Continental Event Illuminating the Moxi Seismic Gap. *Seismol. Res. Lett.*, **94**, 2129–2142 (2023).
- Li, Y. C. et al. Coseismic slip model of the 2022 Mw 6.7 Luding (Tibet) earthquake: Pre- and post-earthquake interactions with surrounding major faults. *Geophysical Research Letters*, **49**, eGL102043 (2022).
- Xu, X. W. et al. Three-dimensional fault model and features of chained hazards of the Luding MS 6.8 earthquake, Sichuan province, China. *Earthq. Res. Adv.* **4**, 100326 (2024).
- Chen, Y. T., Yang, Z. X., Zhang, Y. & Liu, C. From 2008 Wenchuan earthquake to 2013 Lushan earthquake (in Chinese). *Scientia Sinica Terrae*, **43**, 1064–1072 (2013).
- Zhang, Y. J., Guo, R. M., Sun, H. P., Liu, D. C. & Zahradnik, J. Asymmetric bilateral rupture of the 2022 Ms 6.8 Luding earthquake on a continental transform fault, Tibetan border, China. *Seismological Soc. Am.* **94**, 2143–2153 (2023).
- Li, Y. C., Shan, X. J., Gao, Z. Y. & Huang, X. Interseismic coupling, asperity distribution, and earthquake potential on major faults in southeastern Tibet. *Geophysical Research Letters*, **50**, eGL101209 (2023).
- Replumaz, A., Lacassin, R., Tapponnier, P. & Leloup, P. H. Large river offsets and Plio-Quaternary dextral slip rate on the red river fault (Yunnan, China). *J. Geophys. Research: Solid Earth*, **106**, 819–836 (2001).
- Xu, X. W., Wen, X. Z., Chen, G. H. & Yu, G. H. Discovery of the Longriba fault zone in Eastern Bayan Har block, China and its tectonic implication. *Sci. China Ser. D: Earth Sci.* **51**, 1209–1223 (2008).
- Tan, X. B. et al. Parallelism between the maximum exhumation belt and the Moho ramp along the Eastern Tibetan plateau margin: coincidence or consequence? *Earth Planet. Sci. Lett.* **507**, 73–84 (2019).
- Gan, W. J. et al. Present-day crustal motion within the Tibetan plateau inferred from GPS measurements. *Journal Geophys. Research: Solid Earth*, **112**, (2007).

33. Wang, M. & Shen, Z. K. Present-day tectonic deformation in continental china: Thirty years of GPS observation and research (in Chinese). *Earthq. Res. China*. **36**, 660–683 (2020).
34. Zhang, P. Z. A study on the present tectonic deformation, strain partitioning and deep dynamic process of West Sichuan region on Eastern margin of Qinghai-Tibet plateau. *Sci. China Ser. D: Earth Sci.* **38**, 1041–1056 (2008).
35. Zhang, P. Z. A review on active tectonics and deep crustal processes of the Western Sichuan region, Eastern margin of the Tibetan plateau. *Tectonophysics* **584**, 7–22 (2013).
36. Chen, G. H., Xu, X. W., Wen, X. Z. & Chen, Y. G. Late quaternary slip-rates and slip partitioning on the southeastern Xianshuihe fault system, Eastern Tibetan plateau. *Acta Geologica Sinica-English Ed.* **90**, 537–554 (2016).
37. Ran, Y. K., Chen, L. C., Cheng, J. W. & Gong, H. L. Late quaternary surface deformation and rupture behavior of strong earthquake on the segment North of Mianning of the Anninghe fault. *Sci. China Ser. D: Earth Sci.* **51**, 1224–1237 (2008).
38. Wang, Y. Z. et al. GPS-constrained inversion of present-day slip rates along major faults of the Sichuan-Yunnan region, China. *Sci. China Ser. D: Earth Sci.* **51**, 1267–1283 (2008).
39. Ross, Z. E. et al. Hierarchical interlocked orthogonal faulting in the 2019 Ridgecrest earthquake sequence. *Science* **366**, 346–351 (2019).
40. Waldhauser, F. & Ellworth, W. L. A double-difference earthquake location algorithm: method and application to the Northern Hayward fault, California. *Bull. Seismol. Soc. Am.* **90**, 1353–1368 (2000).
41. Carena, S. & Suppe, J. Three-dimensional imaging of active structures using earthquake aftershocks: the Northridge thrust, California. *J. Struct. Geol.* **24**, 887–904 (2002).
42. Liu, Y. et al. The high-resolution community velocity model V2.0 of Southwest china, constructed by joint body and surface wave tomography of data recorded at temporary dense arrays. *Sci. China Earth Sci.* **66**, 2368–2385 (2023).
43. Freed, A. M. Earthquake triggering by static, dynamic, and postseismic stress transfer. *Annu. Rev. Earth Planet. Sci.* **33**, 335–367 (2005).
44. Stein, R. S. The role of stress transfer in earthquake occurrence. *Nature* **402**, 605–609 (1999).
45. Scholz, C. H. *The Mechanics of Earthquakes and Faulting* p. 439 (Cambridge University Press, 1990).
46. Guo, R. M. et al. Kinematic slip evolution during the 2022 Ms 6.8 Luding, china, earthquake: compatible with the preseismic locked patch. *Geophysical Res. Letters*, **50**, (2023).
47. Liang, H. B. et al. Coseismic slip and deformation mode of the 2022 Mw 6.5 Luding earthquake determined by GPS observation. *Tectonophysics* **865**, 230042 (2023).
48. Barbot, S. & Fialko, Y. Fourier-domain green's function for an elastic semi-infinite solid under gravity, with applications to earthquake and volcano deformation: Fourier-domain elastic solutions. *Geophys. J. Int.* **182**, 568–582 (2010).
49. Li, H. W. & Wu, D. C. The main structural characteristics and activity analysis of the Daduhe fault zone. *J. Yangtze Univ. (Nat. Sci. Edit)*. **11**, 61–63 (2014).
50. Wan, Y. G., Wu, Z. L., Zhou, G. W. & Huang, J. Stress triggering between different rupture events in several earthquakes (in Chinese). *Acta Seismol. Sin.* **22**, 568–576 (2000).
51. King, G. C., Stein, R. S. & Lin, J. Static stress changes and the triggering of earthquakes. *Bull. Seismol. Soc. Am.* **84**, 935–953 (1994).
52. Dreger, D. & Kaverina, A. Seismic remote sensing for the earthquake source process and near-source strong shaking: A case study of the October 16, 1999 Hector mine earthquake. *Geophys. Res. Lett.* **27**, 1941–1944 (2000).
53. Xie, C. D. et al. The effect on the nucleation and failure of Ms7.0 Lushan earthquake induced by the Ms8.0 Wenchuan earthquake (in Chinese). *Chiese J. Geophys.* **57**, 1825–1835 (2014).
54. Xie, C. D., Zhu, Y. Q., Lei, X. L. & Yu, H. Y. Earthquake triggering and stress loading/unloading effect on faults induced by the Ms8.0 Wenchuan earthquake, sichuan, China (in Chinese). *Seismological Geomagnetic Observation Res.* **31**, 12–18 (2010).
55. Zhang, L., Su, J., Wang, W. L., Fang, L. H. & Wu, J. P. Deep fault slip characteristics in the Xianshuihe-Anninghe-Daliangshan fault junction region (eastern Tibet) revealed by repeating micro-earthquakes. *J. Asian Earth Sci.* **227**, 105115 (2022).
56. Hardebeck, J. L., Nazareth, J. J. & Hauksson, E. The static stress change triggering model: constraints from two Southern California aftershock sequences. *J. Geophys. Research: Solid Earth*. **103**, 24427–24437 (1998).
57. Reasenber, P. A. & Simpson, R. W. Response of regional seismicity to the static stress change produced by the Loma Prieta earthquake. *Science* **255**, 1687–1690 (1992).
58. Yi, G. X. et al. Stress state and major-earthquake risk on the Southern segment of the longmen Shan fault zone (in Chinese). *Chin. J. Geophys.* **56**, 1112–1120 (2013).
59. Li, J. Y. et al. Seismogenic depths of the Anninghe-Zemuhe and Daliangshan fault zones and their seismic hazards (in Chinese). *Chin. J. Geophys.* **63**, 3669–3682 (2020).
60. Graham, S. E., Loveless, J. P. & Meade, B. J. A global set of subduction zone earthquake scenarios and recurrence intervals inferred from geodetically constrained block models of interseismic coupling distributions. *Geochemistry Geophys. Geosystems*, **22**, (2021). p.e2021GC009802.
61. Stein, R. S., Barka, A. A. & Dieterich, J. H. Progressive failure on the North Anatolian fault since 1939 by earthquake stress triggering. *Geophys. J. Int.* **128**, 594–604 (1997).
62. Kilb, D., Gombert, J. & Bodin, P. Aftershock triggering by complete coulomb stress changes. *Journal Geophys. Research: Solid Earth*, **107**, (2002).
63. Robinson, R. & Zhou, S. Stress interactions within the tangshan, china, earthquake sequence of 1976. *Bull. Seismol. Soc. Am.* **95**, 2501–2505 (2005).
64. Shan, B., Xiong, X., Wang, R. J., Zheng, Y. & Yang, S. Coulomb stress evolution along Xianshuihe–Xiaojiang fault system since 1713 and its interaction with Wenchuan earthquake, May 12, 2008. *Earth Planet. Sci. Lett.* **377**, 199–210 (2013).

Acknowledgements

We thank the China Scholarship Council for their funding. We thank the Data Management Center of China National Seismic Network and the China Seismic Experiment Site. We thank Dr. Guixi Yi and Dr. Long Zhang for providing seismic data and Dr. Yanchuan Li for providing coupling data of the southeastern margin of the Tibetan Plateau.

Author contributions

F.X.: Writing-original draft, Visualization, Methodology, Investigation, Conceptualization. R.Q.L.: Writing-original draft, Visualization, Methodology, Conceptualization, Resources, Funding acquisition. J.Y.Z.: Writing-original draft, Writing-review & editing. Y.K.: Writing-original draft, Writing-review & editing. Y.D.L.: Writing-review & editing. X.H.Y.: Methodology, Conceptualization. G.S.L.: Investigation, Writing-review & editing. W.W.: Methodology, Funding acquisition. Z.W.G.: Writing-review & editing.

Funding

National Key R&D Programs of China, 2023YFC3012000. National Key R&D Programs of China,

2021YFC3000600.

Declarations

Competing interests

The authors declare no competing interests.

Additional information

Supplementary Information The online version contains supplementary material available at <https://doi.org/10.1038/s41598-025-11553-2>.

Correspondence and requests for materials should be addressed to R.L. or J.Z.

Reprints and permissions information is available at www.nature.com/reprints.

Publisher's note Springer Nature remains neutral with regard to jurisdictional claims in published maps and institutional affiliations.

Open Access This article is licensed under a Creative Commons Attribution-NonCommercial-NoDerivatives 4.0 International License, which permits any non-commercial use, sharing, distribution and reproduction in any medium or format, as long as you give appropriate credit to the original author(s) and the source, provide a link to the Creative Commons licence, and indicate if you modified the licensed material. You do not have permission under this licence to share adapted material derived from this article or parts of it. The images or other third party material in this article are included in the article's Creative Commons licence, unless indicated otherwise in a credit line to the material. If material is not included in the article's Creative Commons licence and your intended use is not permitted by statutory regulation or exceeds the permitted use, you will need to obtain permission directly from the copyright holder. To view a copy of this licence, visit <http://creativecommons.org/licenses/by-nc-nd/4.0/>.

© The Author(s) 2025